Flow Turbulence Combust (2015) 94:415–438
DOI 10.1007/s10494-014-9586-9

A Numerical Simulation of the Effects of Swirling Flow on Jet Penetration in a Rotating Channel

Nabeel Al-Zurfi · Ali Turan

Received: 9 January 2014 / Accepted: 10 November 2014 / Published online: 20 November 2014

Abstract The hydrodynamic effects of a jet in a swirling cross-flow problem, which is related to gas turbine blades film cooling, were numerically simulated using large eddy simulation with artificial inflow boundary conditions. The purpose of this study is to investigate the effects of swirling flow on a jet effusing from an inclined hole in a rotating channel. The finite volume method and the unsteady PISO algorithm were applied on a non-uniform staggered grid. The work is naturally divided into two main parts. The first part (the swirl flow generator), is a channel rotates axially to generate a turbulent swirling flow at different values of swirl number (SN) of 0.0, 0.15, 0.3, and 0.5 while the second part (test section), is a channel rotating about a parallel axis to investigate the interaction of a square jet with the turbulent swirling flow, generated by the first part, for the prediction of the film cooling under rotating conditions. Four different values of rotation number (Ro) were applied to the test section. The air jet was injected at 30 deg in the streamwise direction, at a velocity ratio of 1.0 and a jet Reynolds number of 4,700, based on the hole width and the jet exit velocity. It was found that the swirling flows primarily displayed the velocity profile of a forced vortex. Weak reverse flow was observed near the main vortex core, which moved in the direction of the swirl and deformed the kidney shape of the Counter Rotating Vortex Pair. As SN increases ($SN > 0$), the jet trajectory twists in an increasingly x-axis direction due to the centrifugal force effects of the swirl flow, and shifts from the centreline of the channel

---

N. Al-Zurfi (✉) · A. Turan
School of Mechanical, Aerospace and Civil Engineering, The University of Manchester, Manchester, UK
e-mail: nabeel.al-zurfi@postgrad.manchester.ac.uk

A. Turan
e-mail: A.Turan@manchester.ac.uk

N. Al-Zurfi
Mechanical Engineering Department, College of Engineering, University of Kufa, Najaf, Iraq

to the right-hand side (Z/D = + 1.5). Also, it was shown that rotation has a strong impact on the mixing behaviour and film cooling effectiveness. Finally, it was concluded that the film cooling decreases rapidly as SN increases.

Keywords Swirl flow · Jet into cross-flow · Rotation · Large eddy simulation · Film cooling effectiveness

Nomenclature

C_s	Smagorinsky model constant.
d	Film hole width, ***mm.***
DR	Density ratio.
M_w	Gas molecular weight.
P	Pressure, $N.m^{-2}$.
Pr	Prandtl Number.
Pr_t	Turbulent Prandtl Number.
R	Universal gas constant.
Re	Reynolds number.
Ro	Rotation number.
SGS	Sub grid-scale.
SN	Swirl number.
t	Time, ***s.***
T	Local fluid temperature, ***K.***
u_τ	Friction velocity, ***m/s.***
u^+	Velocity normalized by friction velocity.
u, v, w	Dimensional velocity components, ***m /s.***
VR	Velocity ratio.
X	Spatial vector.
x, y, z	Dimensional coordinates in streamwise, normal, and spanwise directions, respectively, ***m***.
y^+	Dimensionless wall distance.

Greek symbols

Δ	Filter width.
Δt	Time step, ***s.***
$\Delta x, \Delta y, \Delta z$	Mesh spacing in the x, y, z directions, ***m.***
η	Local film cooling effectiveness.
$\bar{\eta}$	Spanwise-averaged film cooling effectiveness.
ρ	Fluid density, $kg\ /m^3$.
τ_w	Wall shear stress, $N.m^{-2}$.
μ	Dynamic viscosity, $N \bullet s\ /m^2$.
μ_{sgs}	Sub-grid scale eddy viscosity, $N \bullet s/m^2$
v	Kinematics viscosity, m^2/s.
Ω	Rotating speed, ***rad/s***

Subscripts

i, j,k	directions i,j,k.
rms	Root mean square.
∞	Free stream.

Mathematical Accents

-	Filtered (LES) quantity.
\	Fluctuating quantity.
<>	Time averaging.
<<>>	Time and spatial averaging.

1 Introduction

The jet in a cross-flow (JICF) problem is relevant to many engineering applications, such as film cooling of turbine blades, combustion chamber fuel injection, wall cooling, fluid mixing and smokestack pollution dispersion. The gas turbine industry has been making efforts to improve the power and thermal efficiency of gas turbine engines by increasing the turbine inlet temperature. Therefore, it has become increasingly necessary to protect the gas turbine blades from oncoming hot combustion gases using a thin fluid film that surrounds the blade. To achieve such a protective layer, cooler fluid is injected into the hot cross-flow through the small holes placed on the surface of the blade. As a result, blades will be able to perform and survive long operating periods at temperatures above their melting point. Therefore, JICF problems have been simulated in various numerical and experimental studies. Most early studies into film cooling were driven by applications other than gas turbine cooling, beginning in the 1930s with systematic studies of chimney plumes [3, 27], the high-temperature gaseous environment around vehicles, surfaces containing plasma jets, rockets, or flame tube devices.

Recent developments in numerical tools make the Computational Fluid Dynamics (CFD) technique capable of providing more detailed and comprehensive analysis of the flow physics and heat transfer mechanism, which can help in improving the efficiency of film cooling. Several factors including the physical and geometrical quantities affecting that efficiency have been investigated so far. Some of the most important of these are reviewed below.

1.1 Density ratio effects

The effects of the density ratio on film-cooling effectiveness have been investigated experimentally and numerically by several researchers. Goldstein and Eckert [9] investigated film cooling downstream of a secondary gas injection through a row of holes into the main stream. Freon vapour was used to provide a denser coolant. A mixture of air and Helium, CO_2, or refrigerant F-12 was injected into the main stream by Pedersen et al. [20]. One of the plane walls was equipped with a row of holes with three diameters lateral spacing; the holes were inclined 35 deg into the main stream. The density ratio ranged from 0.75 to

4.17. The results obtained show that the density ratio has a strong effect on the film-cooling effectiveness which reaches a maximum value for velocity ratio between 0.4 and 0.6.

Measurements of cryogenically cooled jets with thermocouple arrangements were performed by Pietrzyk et al. [22]. They used the Laser-Doppler anemometry technique (LDA) to measure the vertical and streamwise components of velocity for the flow field that resulted from cooling the air jet to obtain a density ratio of DR = 2. In addition, Sinha et al. [25] injected cooled air into a main stream for a density ratio between 1.2 and 2.0. They concluded that the film-cooling effectiveness improves with increasing the density ratio.

Holdeman [12] summarised that the mixing of multiple jets with a cross-flow was improved with downstream distance and the effect of density ratio appeared to be small at a constant momentum flux ratio. A transient liquid crystal technique was used by Ekkad et al. [6]. The coolant fluid was injected in a cross-flow with one row of injected holes, which was angled 35 deg to the surface in the streamwise direction. Results showed that the Nusselt numbers decrease with increasing density ratio for a constant blowing ratio. Later, Renze et al. [24] simulated the injection of a CO_2 jet from an inclined pipe at 30 deg into an air stream for a free-stream Reynolds number of 400,000 and different values of velocity ratio of 0.1, 0.28, and 0.48 using the LES approach. The distribution of the mixture-fraction scalar proves the significance of the coherent structures in the dynamic flow field on the mixing process. Moreover, it was observed that the counter-rotating eddies lift the high density jet fluid off the plate at the trailing edge. In a recent study, the LES approach was used by Ramezanizadeh et al. [23] to simulate multiple square jets inclined normally into a main cross-flow, as well as by Farhadi et al. [7] to simulate triple jets, based on the ordinary (single) rectangular jet and combined triple jets (CTJ). The finite volume method and unsteady SIMPLE algorithm technique on a multi-block, non-uniform staggered grid were employed to solve the governing equations. Both simulations were performed for three different density ratios of 0.5, 1, and 2, a velocity ratio of 0.5, and a jet Reynolds number of 4,700. In the case of the multiple jet study, it was observed that a Counter-Rotating Vortex Pair (CRVP) generates on the Y and Z planes and two horse shoe vortices (HSV) appear at the lower corners of the plane beneath the CRVP as the jet penetrates the main stream. Meanwhile, in the CTJ configuration, two small rectangular coolant holes were placed just downstream of the main cooling hole in order to enhance film-cooling effectiveness. The results showed that any increase in the density ratio will increase the penetration of the jet into the cross-flow. For a constant velocity ratio, the centreline and spanwise averaged film-cooling effectiveness increases with increasing density ratio.

1.2 Blowing ratio effects

Blowing ratio effects have been widely investigated to find out how to achieve optimum film-cooling effectiveness using a minimum amount of coolant fluid.

Andreopoulus and Rodi [1] measured the flow field generated by a jet issuing from a circular outlet into a cross-stream at different velocity ratios (VR = 0.5, 1, and 2) using hot-wire probes. Their results showed the strong influence of velocity ratio on film cooling, where the jet penetrates further into the cross-stream as VR increases and the wake region increases with increasing VR.

Nishiyama et al. [19] performed a study of a two-dimensional jet issuing through a 40: 1 aspect ratio slot normally into a cold cross-flow at blowing ratios of 0.2, 1.5 and 3.0. They concluded that the rate of mixing between jet and cross-flow reduces as the blowing ratio increases. Ligrani and Lee [17] carried out an experimental study of the flow downstream of two staggered rows of film-cooling holes at high blowing ratios ranging from 0.5 to 4.0

and with a density ratio of 1.0. The holes were spaced 3d apart in the spanwise direction and were inclined 24 deg along the mainstream direction, with an additional angle of orientation 50.5 deg in the spanwise direction. The highest value of the spanwise averaged film-cooling effectiveness was measured at a blowing ratio of 0.5. Also, the results showed that the spanwise averaged film-cooling effectiveness and flow characteristics change by a significant amount as the blowing ratio increases. An extensive experimental investigation and a companion numerical simulation using a low-Re k-ε was conducted by Ajersch et al. [2]. The study investigated the complex flow created by a row of six square jets blowing at 90 deg into a cross flow. Three values of velocity ratio were considered between 0.5 and 1.5. The time-averaged streamwise velocity in the jet wake was over predicted and the recirculation region behind the jet was found to be smaller and closer to the surface than that observed in the measurements. The counter rotating vortex pair is observed for VR $=$ 1.5 and 1.0, while the jet is too weak to penetrate through the upstream turbulent boundary layer for VR $=$ 0.5.

The flow field characteristics of a square jet injected into a cross-flow were also examined by Findlay et al. [8] at different blowing ratios (0.5, 1, and 1.5) with a density ratio of 1.0. The jet injection was considered perpendicular and was angled 30 deg to the surface in the streamwise and spanwise directions, respectively. The measurements showed that the streamwise injection cases improved the film-cooling effectiveness significantly. An unstructured grid, fully explicit, and a time-marching code with multiple grids were employed by Walters and Leylek [32] to analyse the flow physics of a jet inclined into cross-flow. Three different blowing ratios from 0.5 to 2.0 were considered. They concluded that the film-cooling performance is affected by the counter-rotating secondary flow structure downstream of the jet exit in the streamwise injection cases, which can be improved by controlling the strength of the counter-rotating vortex pair. In a recent investigation, Yao et al. [33] used the direct numerical simulation (DNS) to predict the flow structures emerged from the interaction of a single square jet issuing into a cross-flow at a velocity ratio of 2.5 and a free stream Reynolds number of 225. Three different kinds of jet geometries have been considered, normal jet, inclined jet at angles of 30 and 60 deg, and round and elliptic jets at an angle of 90 deg. It was found that the jet geometry has a strong effect on the jet penetration, the analysis showed that the jet penetrates deeper into the cross flow field for the normal jet. Also, the maximum lifted-off effect was caused by the elliptic jet hole shape compared with the three hole configurations.

1.3 Rotation effects

Very few experimental studies observing the rotating effects are available, due to the difficulties in conducting this type of experiment. However, an interesting study was carried out by Tao et al. [28] to investigate the rotation effects on film cooling over a flat blade using a liquid-crystal technique. Different rotational speeds ranging from 0 to 1000 rpm were examined. The coolant fluid was injected from a single hole, angled 30 deg to the surface in the hot mainstream. The results indicated that as the rotational speed increases the adiabatic film-cooling effectiveness increases for $\Omega \leq 500$ rpm, while it decreases for $\Omega > 500 - 600$ rpm on the pressure side. However, this behaviour is not found on the suction side, as the adiabatic film-cooling effectiveness is not sensitive to the rotational speed. Recently, a numerical study was undertaken by Li et al. [16]. The authors simulated the effects of rotational speed on the film-cooling effectiveness of rotating blades with compound-angle holes using the turbulence model of the realisable k-ε two-equation method. Three values of rotating speed between 0 to 1000 rpm have been considered. They confirmed that the rotation deflects the film cooling toward the blade tip. Also, the smaller value of jet angle on the leading edge improves the film-cooling effectiveness at a blowing ratio of 1.0 and a rotational speed of 200 rpm.

To avoid complexities arising from the curvature of the surface of the turbine blade, researches into film cooling over a flat surface are common. Flat surface models can be used to study the effects of individual parameters with relative ease and are less expensive. Early studies have proved that the results obtained on simple flat surface models can be applied to real engine design with slight corrections, Han et al. [10].

On the other hand, the impact of the swirled hot gas cross-flow on the penetration behaviour and cooling efficiency of a cooling film is an area of interest. Within modern gas turbine combustion chambers designed for lean combustion the air - fuel mixing process is done by the fuel injectors only and there is no need to use additional mixing ports. Swirl stabilization is used within this kind of mixing process. The swirl flow interacts with near wall cooling flows which assure a proper wall cooling near the fuel injector.

Therefore, the aim of the present study is to investigate the effects of swirling flow on a jet issuing in a rotating channel, rotates about a parallel axis, using the large eddy simulation technique. The jet was injected at 30 deg in the streamwise direction at a constant temperature of 307 k through a single square hole. Simulations were performed for four different rotation numbers (Ro) of 0, 0.006042, 0.12084, and 0.18126 with a velocity ratio (VR) of 1.0, and a jet Reynolds number (Re) of 4,700.

2 Mathematical and Numerical Formulations

2.1 Governing equations

As is well known, the governing equations for large-scale motion (resolved scales) can be obtained by applying a spatial filter to the mass, momentum, and energy conservation equations (indicated by an overbar). With a constant filter width, the resulting equations in tensor notations for a three-dimensional, time-dependent, and incompressible Newtonian fluid are:

$$\frac{\partial \rho}{\partial t}+\frac{\partial \rho \bar{u}_i}{\partial x_i}=0 \tag{1}$$

$$\frac{\partial(\rho \bar{u}_i)}{\partial t}+\frac{\partial(\rho \bar{u}_i \bar{u}_j)}{\partial x_j}=-\frac{\partial \bar{p}}{\partial x_i}+\frac{\partial}{\partial x_j}\left(\mu\left(\frac{\partial \bar{u}_i}{\partial x_j}+\frac{\partial \bar{u}_j}{\partial x_i}\right)-\rho\tau_{ij}\right)-\rho\varepsilon_{ikj}\varepsilon_{jlm}\Omega_k\Omega_l X_m-2\rho\varepsilon_{ikj}\Omega_k\bar{u}_j \tag{2}$$

$$\frac{\partial(\rho \bar{T})}{\partial t}+\frac{\partial(\rho \bar{T}\bar{u}_i)}{\partial x_i}=\frac{\partial}{\partial x_i}\left(\frac{\mu}{\mathrm{Pr}}\frac{\partial \bar{T}}{\partial x_i}-\rho q_i\right) \tag{3}$$

where $\bar{u}_i$ is the filtered velocity, $\bar{p}$ is the filtered pressure, Ω is the constant angular velocity of the rotating channel (test section), ε_{ijk} is the Levi-Civita's alternating tensor, $\bar{T}$ is the filtered temperature, and μ is the dynamic viscosity of the fluid, which is obtained using Sutherland's law, Peyret [21]:

$$\mu=\mu_\infty . T^{1.5}\left[1+\frac{110.4}{T_\infty}\right]/\left[T+\frac{110.4}{T_\infty}\right]$$

The fourth term on the right-hand side (centrifugal force) of Eq. 2 was divided into two terms: constant density terms ($\rho_o\Omega\times\Omega\times r$) and centrifugal buoyancy force term ($\rho_o\beta\Delta T\Omega\times\Omega\times r$). The pressure gradient balances the constant density term and would not influence the velocity and temperature distribution. Therefore, the constant density term can be merged into the pressure gradient term ($\bar{P}_{eff} = \bar{p} - \frac{1}{2}\rho_o\Omega^2 r^2$). That means the velocity and temperature distribution would be only changed by the centrifugal buoyancy and coriolis forces (see Fig. 1). On the other hand, the temperature differences of the jet into cross-flow cause density variations, therefore, the ideal gas law for an incompressible Newtonian flow was used in order to compute the spatial and the temporal density variations throughout the computational domain every time step except the boundary values.

$$\rho = \frac{p}{\frac{R}{M_w}\bar{T}}$$

The effects of the smaller unresolved scales are presented in the following SGS stress and SGS heat flux, which require modelling -:

$$\tau_{ij} = \overline{u_i u_j} - \bar{u}_i \bar{u}_j$$

$$q_i = \overline{T u_i} - \bar{T}\bar{u}_i$$

The subgrid scales can be calculated with models based on physical reasoning and empirical information. Smagorinsky [26] suggested relating the SGS to the resolved scales by an eddy viscosity model:

$$\tau_{ij} - \frac{1}{3}\delta_{ij}\tau_{kk} = -2\nu_{sgs}\bar{S}_{ij} \tag{4}$$

where $\bar{S}_{ij}$is the resolved strain rate tensor, $\delta_{ij}$is the Kronecker delta, and ν_{sgs} is the subgrid kinetic eddy viscosity. The contribution from the diagonal term proportional to τ_{kk} in Eq. 4 was added into the reduced pressure and does not need to be accounted for:

$$\bar{P}_r = \bar{p}_{eff} + \rho(\frac{1}{3}\tau_{kk})$$

The eddy viscosity in Eq. 4 is obtained by assuming that the turbulent dissipation is in equilibrium with the turbulent energy production. This yield an expression:

$$\nu_{sgs} = l_s^2\left|\bar{S}\right| = (C_s\Delta)^2\left|\bar{S}\right| \tag{5}$$

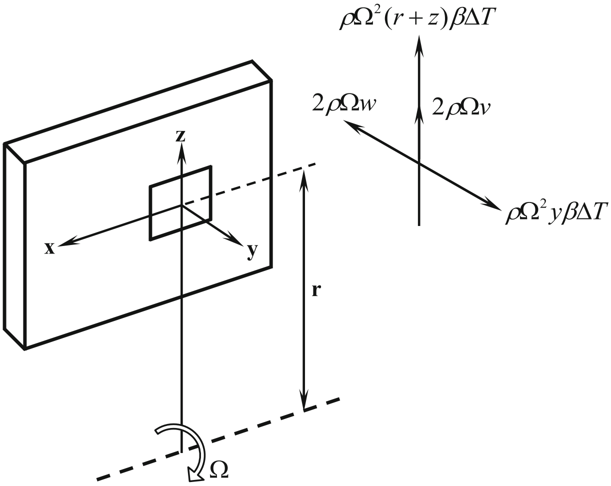

Fig. 1 Sketch map of the Coriolis force and centrifugal induced buoyancy force

where $l_s = C_s\Delta$ is the length scale, C_s is Smagorinsky constant, and $\bar{S} = \sqrt{2\bar{S}_{ij}\bar{S}_{ij}}$ is a measure of the velocity gradient defined as $\bar{S}_{ij} = \frac{1}{2}\left(\frac{\partial \bar{u}_i}{\partial x_j} + \frac{\partial \bar{u}_j}{\partial x_i}\right)$.

Also, the SGS heat flux vector (q_i) is modelled using a gradient-diffusion hypothesis as:

$$q_i = -\frac{\nu_{sgs}}{\mathrm{Pr}_t}\frac{\partial \bar{T}}{\partial x_i}$$

The filter width can be defined as ($\Delta = V^{1/3}$) with V denoting the control volume, which yields a filter width of $\Delta = (\Delta x \Delta y \Delta z)^{1/3}$ for a Cartesian grid. Since the computational grid is clustered near the walls and jet region. This would require a non uniform filter cut-off width (function of space) in the computational domain. But, as the filter width is a function of space, the filtering operation on spatial differentiation does not commute and the commutation error arises. The commutation error is proportional to the gradient of the filter width ($\frac{d\Delta}{dy}$). In order to keep the commutation error to a minimum, the expansion or compression of the non-uniform grid should be smooth, Molla [18]. In the present work, the mesh expansion ratios lie between 0.833 and 1.2, the grid spacing varies smoothly, so that ($\frac{d\Delta}{dy}$) is small.

A theoretical value of $C_s = 0.1$ is the most appropriate and commonly used for homogeneous isotropic turbulence and has been found to yield the best results for a wide range of simulating turbulent flow with LES, Jiang and Lai [14]. However, these circumstances do not pertain to the viscous wall region and one obvious defect of this basic form that the eddy viscosity does not vanish at solid walls where the flow is, effectively, laminar. Consequently, the constant value of C_s leads, incorrectly, to a non-zero residual viscosity and shear stress at the wall. In order to reduce the excessive eddy viscosity in the near-wall regions, the Van Driest damping function, Van Driest [29], was used to specify l_s as:

$$\nu_{sgs} = \left[C_s\Delta\left[1 - \exp(-y^+/A^+)\right]\right]^2 \left|\bar{S}\right|$$

where $y^+ = yu_\tau/\nu$ is the dimensionless distance from the wall and $A^+ \approx 26$ is a dimensionless constant.

2.2 Physical domain and boundary conditions

To generate a turbulent swirling flow, which interacts with the coolant jet inside the test section, the computational domain is separated into two parts: a swirl flow generator (part I - this is not presented in this study) and a test section (part II), as shown in Fig. 2a. At the inlet section of the first part of the domain (Part I), the mean velocities are set as $V_{in} = W_{in} = 0$ and the 1/7 power law velocity profile was used for the x-velocity component. The swirl flow generator is a long square channel, rotating axially to generate a turbulent swirl flow field which feeds the second part (or test section). In general, the flow downstream of the inlet boundary is highly dependent on the conditions at the entrance, making it necessary to produce a realistic time series of turbulent fluctuations that are in equilibrium with the mean velocity. The efficiency of LES as a predictive tool is partly governed by the quality of the inflow conditions. Therefore, in-flow fluctuation velocity fields (u', v', w') were created at the y-z plane of Part I inlet using the synthesised turbulence method. A fluctuating velocity field is generated each time step that are independent of each other and their time correlation will thus be zero. This is unphysical. To create correlation in time, new fluctuating velocity fields, $(U_i')^n$, are computed based on an asymmetric time filter:

$$(U_i')^n = a(U_i')^{n-1} + b(u_i')^n$$

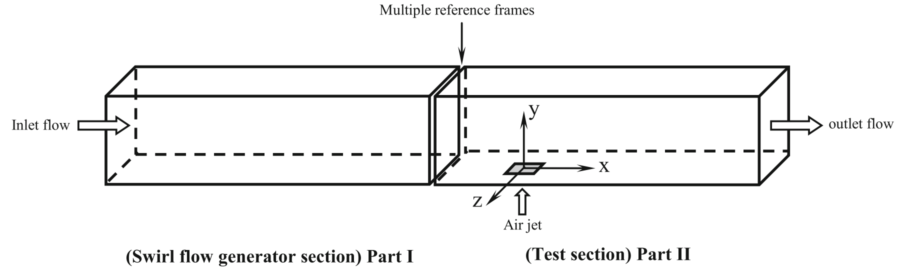

a) The swirl flow generator and test section

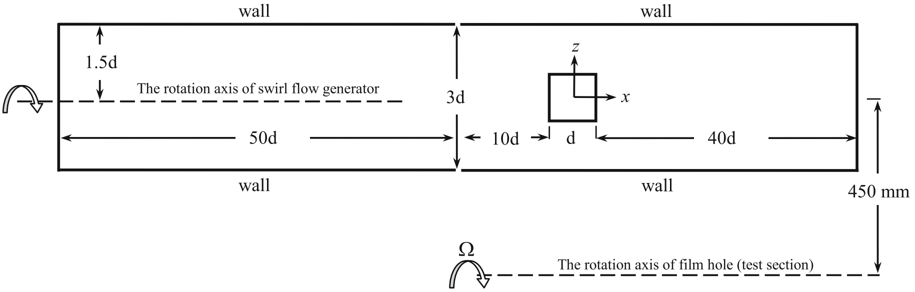

b) Top view of computational domain

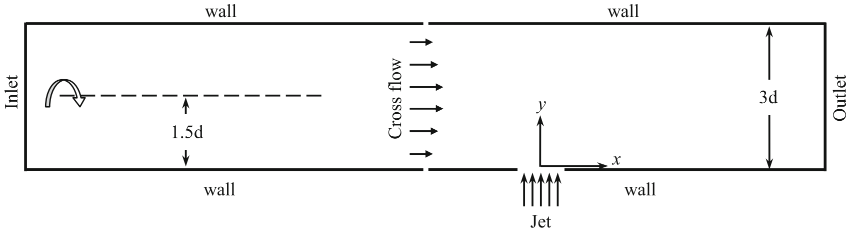

c) Side view of computational domain

Fig. 2 Computational domain and the boundary conditions used

Where n is the time step number, a and b are constant coefficients taken as $a = \exp(-\Delta t/\iota)$ and $b = (1-a^2)^{0.5}$, respectively. Consequently, the instantaneous velocity at the inflow is prescribed as, Davidson and Billson [4] and Davidson [5]:

$$\begin{aligned} \bar{u}(0,y,z,t) &= U_{in}(y) + u'_{in}(y,z,t) \\ \bar{v}(0,y,z,t) &= V_{in}(y) + v'_{in}(y,z,t) \\ \bar{w}(0,y,z,t) &= W_{in}(y) + w'_{in}(y,z,t) \end{aligned} \tag{6}$$

On the other hand, the test section (the area of interest in this study) was used to simulate a coolant jet emanating from a square hole into a hot swirling cross-flow (the mainstream), which was generated by the first part of the domain, using LES method. The injection hole is placed symmetrically (Fig. 2b & c) with respect to the width of the channel floor (or test section). A Cartesian coordinate system is considered, where the origin is at the centre of the square hole, coinciding with the test section floor. The x-axis is along the direction of mainstream (also the direction of rotation axis of test section), the y-axis is perpendicular to the wall, and z-axis is along the lateral direction. The length of test section is 51d and its cross-sectional area is 3d×3d, while the width of film hole is d = 12.7 mm. The rotational radius of the film hole was 450 mm. The outlet section was placed sufficiently far away (40d) from the jet exit. The temperature of mainstream was 319 k, while the temperature of coolant was 307 k. 5 % turbulence intensity was assumed for both mainstream and coolant. No slip and adiabatic boundary condition were applied on the wall boundary while at the outlet the normal gradient of all variables was prescribed as zero. The conduction and radiation heat losses were neglected.

The simulation of the test section configuration was carried out for four different rotating speeds were 0, 250, 500, and 750 rpm and corresponding rotation numbers Ro ($\Omega d/u_\infty$) are 0, 0.06042, 0.12084, and 0.18126 respectively, with a velocity ratio of VR (v_j/u_∞) $= 1.0$ and a Reynolds number Re ($v_j d/\nu$) of 4700, which were based on the hole width and the jet exit velocity. An air jet was injected at 30 deg in the streamwise direction with a density ratio DR (ρ_j/ρ_∞) $= 1.04$.

As the plenum pipe was not modelled in all the cases, the inclination was given by specifying the velocity components under the velocity specification method. At the test section inlet, four different swirl number values SN of 0.0, 0.15, 0.3, and 0.5, generated by Part I, were specified, whereas a uniform flow at the jet inlet was implemented, according to the work of Ramezanizadeh et al. [23].

2.3 Configuration, grid, and boundary treatments

As the grid resolution increases, more scales are resolved by the grids and fewer are modelled using the SGS term, which leads to better and more accurate predictions. Therefore, prior to the actual numerical simulation, a grid independence study for the conditions of SN = 0, Ro = 0, and SN = 0.15, Ro = 0.06042 was performed by using five different grid arrangements (for test section only) with 227500, 460350, 750750, 962000, and 1508000 cells, as shown in Table 1.

The swirl flow generator computational domain consists of 0.754 million cells and do not change since this study mainly focus on the film cooled channel (test section).

In both cross flow and jet flow blocks, grid refinement near the wall and jet region was performed using the following algebraic stretching function, Hoffmann and Chiang [11]:

$$y = H\frac{(2\alpha+\beta)\left[(\beta+1)/(\beta-1)\right]^{(\xi-\alpha)/(1-\alpha)}+2\alpha-\beta}{(2\alpha+1)\left[1+\left[(\beta+1)/(\beta-1)\right]^{(\xi-\alpha)/(1-\alpha)}\right]} \tag{7}$$

where ξ and β are the metric and the clustering coefficient, respectively.

Three blocks were used in order to distribute the grids throughout the computational domain: upstream (block I), in the jet region (block II), and downstream (block III). For all blocks, the grid was clustered symmetrically in Y-direction using Eq. 7 for $\alpha = 0.5$. Also, grid refinement was performed in X direction in the cross flow block. That is, the grid was clustered close to the jet exit and was expanded away from it using Eq. 7 for $\alpha = 1.0$.

The comparisons were made using time-averaged streamwise velocity and turbulent kinetic energy profiles at different positions after the jet exit (X/D = 0.0, 1.0, and 5.0, for Z/D = 0.0), as shown in Fig. 3. Based on these comparisons, the fifth grid was selected. With the current grid resolution, y+ values on the lower wall are kept to be less than 1.0 to be able to resolve the viscous sub layer of the area of interest.

A time step size of $\sim 1\times10^{-4}$s was used at the beginning of the simulations to advance the flow calculations in the first 5000 iterations (time steps), then the time step size was

Table 1 Different grid arrangements for both cross-flow and jet regions (test section)

Grid case	Cross-flow and jet regions	NI	NJ	NK	Total number of grids
1	Block I (upstream of the jet)	35	70	8	227,500
	Block II (jet region)	10		10	
	Block III (downstream of the jet)	80		8	
2	Block I (upstream of the jet)	50	90	11	460,350
	Block II (jet region)	12		11	
	Block III (downstream of the jet)	93		11	
3	Block I (upstream of the jet)	55	110	13	750,750
	Block II (jet region)	13		13	
	Block III (downstream of the jet)	107		13	
4	Block I (upstream of the jet)	60	130	13	962,000
	Block II (jet region)	15		14	
	Block III (downstream of the jet)	110		13	
5	Block I (upstream of the jet)	60	130	19	1,508,000
	Block II (jet region)	18		20	
	Block III (downstream of the jet)	122		19	

reduced gradually to $\sim 3 \times 10^{-5}$s in order to keep the Courant number (CFL) lower than 1.0.

2.4 Numerical schemes

An in-house FORTRAN code was modified and extended by the authors in order to solve the current problem. The code is fully implicit and second-order accurate in both space and time. The discretisation of the convective terms was carried out using a third-order scheme, as put forward by Farhadi et al. [7]. In addition, a second-order temporal differencing scheme is necessary for improved performance. Therefore, a second-order accurate three-point backward difference approximation was used, as recommended by Versteeg and Malalasekera [30], except for the first time step of the simulations, where a first-order time discretisation was used, as only two time levels were available. The finite volume approach was applied to a non-uniform staggered grid in order to discretise the filtered partial differential Eqs. 1–3 to yield a system of quasi-linear algebraic equations.

The problem of pressure-velocity coupling was solved according to the unsteady PISO algorithm of Issa [13]. To solve the resulting discretised algebraic equations, the Cycle-Tri-Diagonal-Matrix Algorithm (CTDMA) was used. The set of algebraic equations were simultaneously solved, and the convergence was measured in terms of the maximum change allowed in each variable during any iteration, where the maximum value was taken to the order of 1×10^{-5} for all variables.

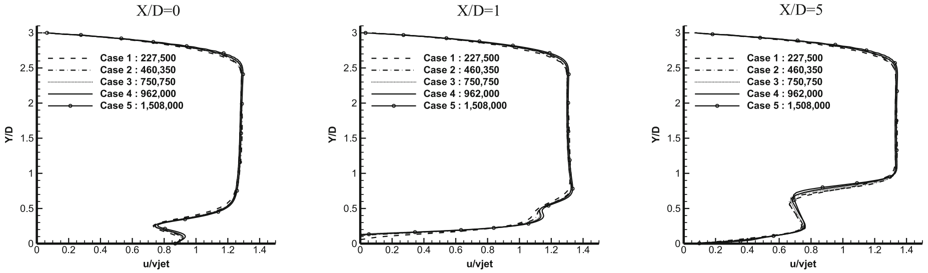

a) U-velocity profiles for SN=0 and Ro=0.

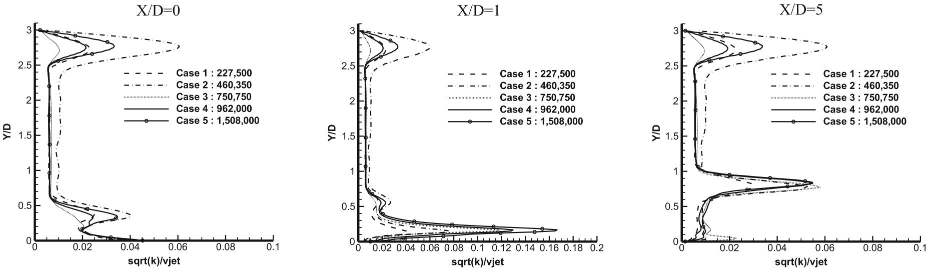

b) Turbulence kinetic energy profiles ($\sqrt{k}\,/\,v_j$) for SN=0 and Ro=0.

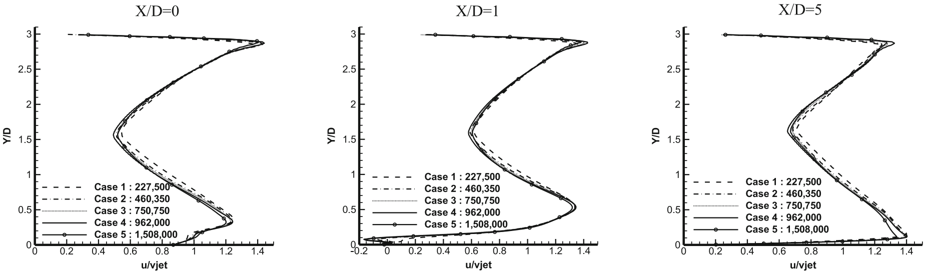

c) U-velocity profiles for SN=0.15 and Ro=0.06042

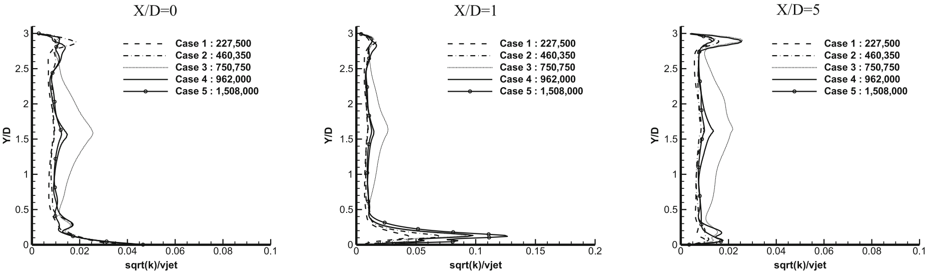

d) Turbulence kinetic energy profiles ($\sqrt{k}\,/\,v_j$) for SN=0.15 and Ro=0.06042 .

Fig. 3 Grid resolution study using time averaged streamwise velocity profiles and time averaged kinetic energy profiles at different positions for $Z/D = 0.0$

3 Validation of the Numerical Method

To examine the present computation, the time-averaged streamwise velocity profiles in different X-locations after the jet exit (X/D = 0.0, 1.0, 3.0, and 5.0, for Z/D = 0.0) were compared with the experimental and computational results of Ajersch et al. [2] for the condition of VR = 0.5, SN = 0.0, and Ro = 0.0. These comparisons were performed to show the ability of the present LES computations in capturing the flow and the mixing characteristics. Profiles of streamwise velocity at X/D = 0.0, 1.0, 3.0, and 5.0, for Z/D = 0.0 are shown in Fig. 4. These profiles show good agreements with experimental results. Although there are small discrepancies as we move away from the jet exit, our results predict the trends much better than the computational results of Ajersch et al. [2].

In regards to the rotational effects on fluid flow and heat transfer, the results computed by the current code for multiple rotation numbers were validated against the DNS data obtained by Kristoffersen and Andersson [15] and the experimental data obtained by Visscher et al.

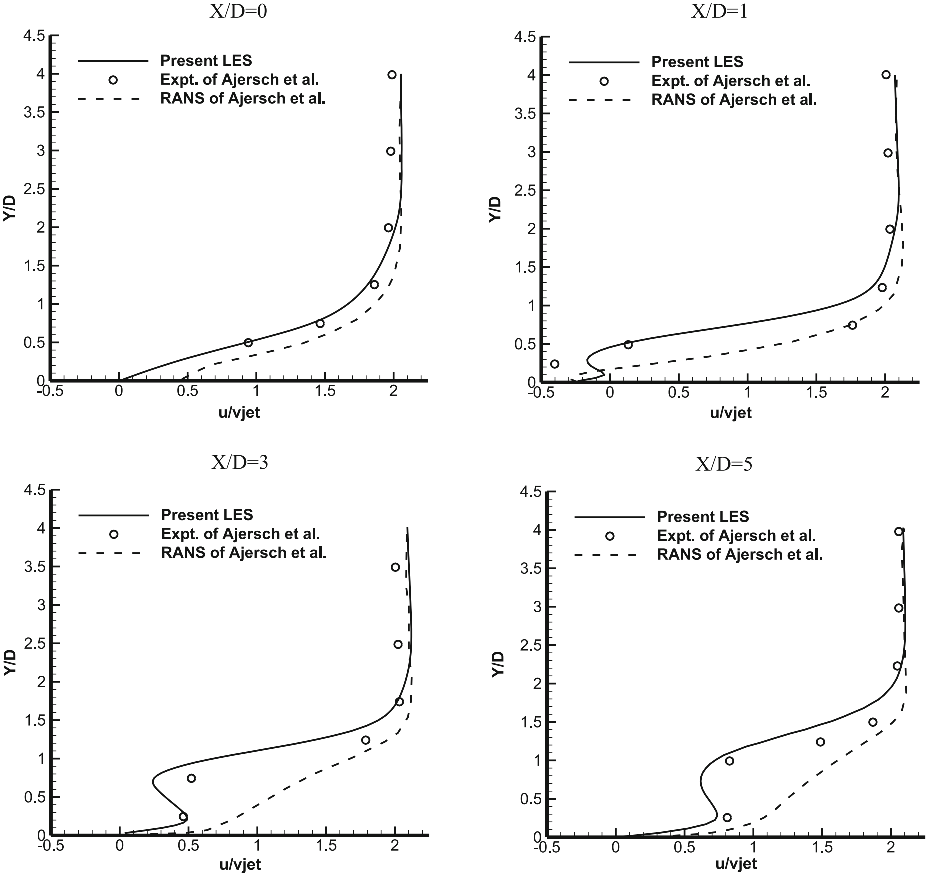

Fig. 4 Comparison of the present time averaged streamwise velocity profiles with the experimental and computational results of Ajersch et al. [2]

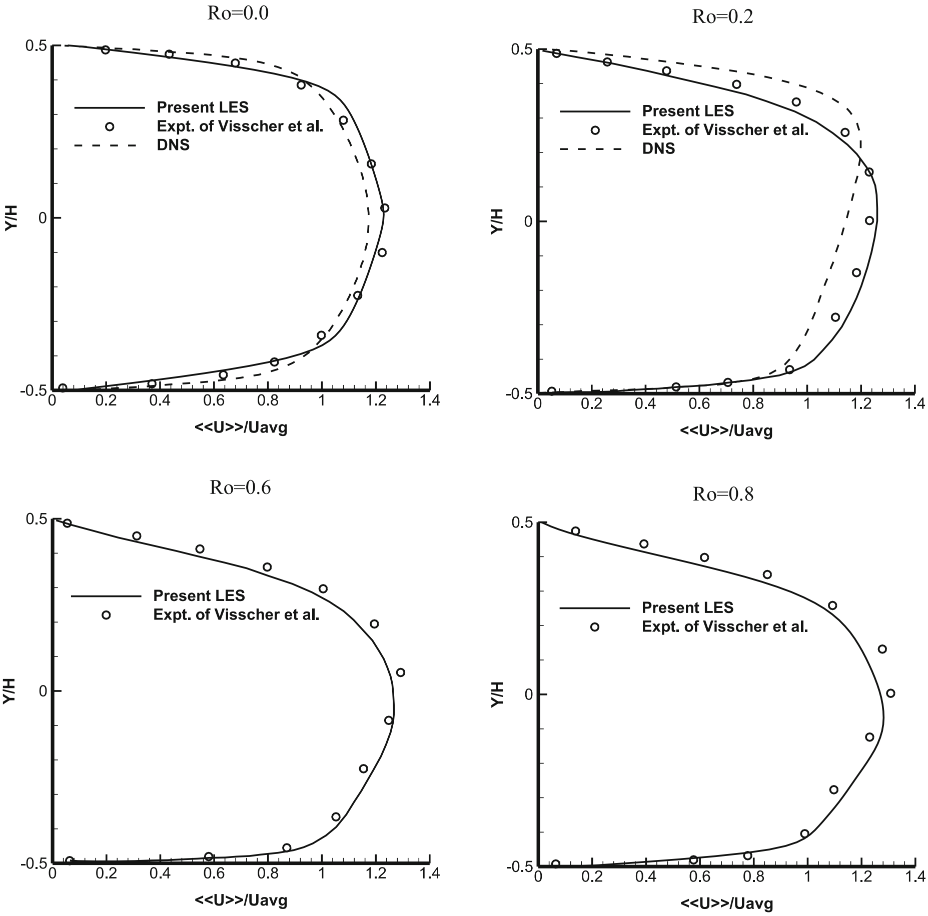

Fig. 5 Mean normalized streamwise velocity for multiple rotation numbers at Re = 5600

[31], where a turbulent flow was examined in a rotating channel for a Reynolds number of 5600. Figure 5 shows a comparison of the time and spatial (in the x-direction) averaged normalised streamwise velocity for rotation numbers ranging from 0 to 0.8. It is obvious that the results predicted by current code and the experimental data are in a good agreement although there are small variances due to the difference in the numerical solution accuracy and the experimental work.

4 Results and Discussion

The initialization period and the statistically stationary state were monitored by the time history of the streamwise velocity at the mid point of the channel (test section). Figure 6 shows that the solution was assumed to be statistically stationary after 10000 iterations (or time steps) from the initial conditions. Initially, mean flow variables (or the first-order statistics) were collected until they converged. As soon as the mean flow variable field

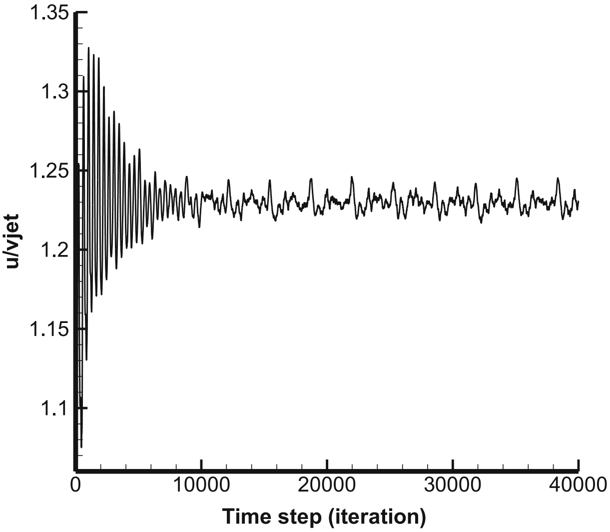

Fig. 6 The time history of streamwise velocity (u/v_{jet}) at the middle of the channel

reached stable (time-independent) values, the turbulence statistics are collected till $\langle u'^2 \rangle$ stabilized as show in Fig. 7. The fluctuating component of velocity (u_i') at any time was calculated by subtracted the mean velocity ($< \bar{u} >$) from the resolved instantaneous velocity (u_i) at each node. These fluctuating components of the velocity field can then be used to calculate the different statistics of the turbulence field at that time step.

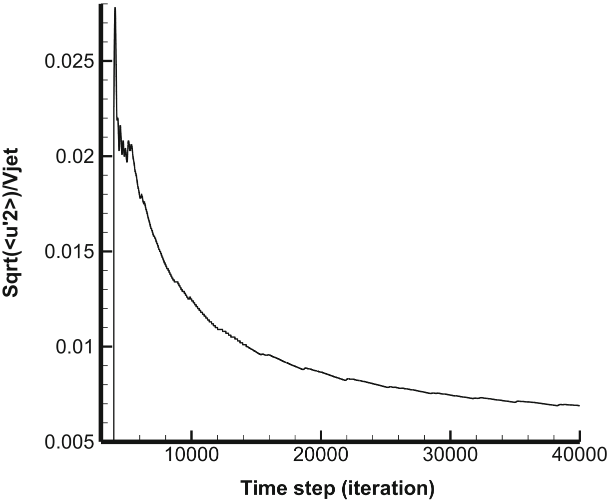

Fig. 7 Streamwise velocity fluctuation ($\sqrt{\langle u'^2 \rangle}/v_{jet}$) at the middle of the channel

4.1 The effects of swirl flow

The swirl number (SN) can be evaluated from the velocity components as:

$$SN = \frac{\iint \sqrt{v^2 + w^2} dydz}{\iint \sqrt{u^2} dydz} \tag{8}$$

Figures 8, 9, and 10 show the time-averaged streamwise velocity and temperature contours for SN = 0, 0.15, and 0.3 at Ro = 0.0. They show the effects of swirl flow on the mixing behaviour of the coolant jet as it interacts with the cross-flow in the y-z plane at different X-locations (X/D = 0.0, 3.0, and 8.0). It is clearly seen that the swirl direction is anti-clockwise. At SN = 0.0 (Fig. 8), no strong interaction between the jet and the approaching boundary layer of the cross-flow can be identified in the region of the jet exit. The jet penetrates smoothly into the cross-flow and is bent after coming out of the injection hole. The jet is symmetrical in the y-z plane at Z/D = 0.0, where a CRVP vortex appears downstream of the jet exit. As X/D increases beyond the jet exit, the boundary layer is lifted by the jet penetration and the CRVP vortex starts to propagate along with a movement in its centre in Y-direction. Downstream of the hole exit (as shown in Fig. 8 at X/D = 8.0), a small reverse flow region can be seen. As SN increases, a strong interaction between the jet and the cross-flow can be seen, as shown in Fig. 9. As X/D increases, the CRVP vortex twists increasingly in anti-clockwise direction and moves away from the lower wall of the channel towards the right side (at Z/D = + 1.5). This behaviour is due to the centrifugal force

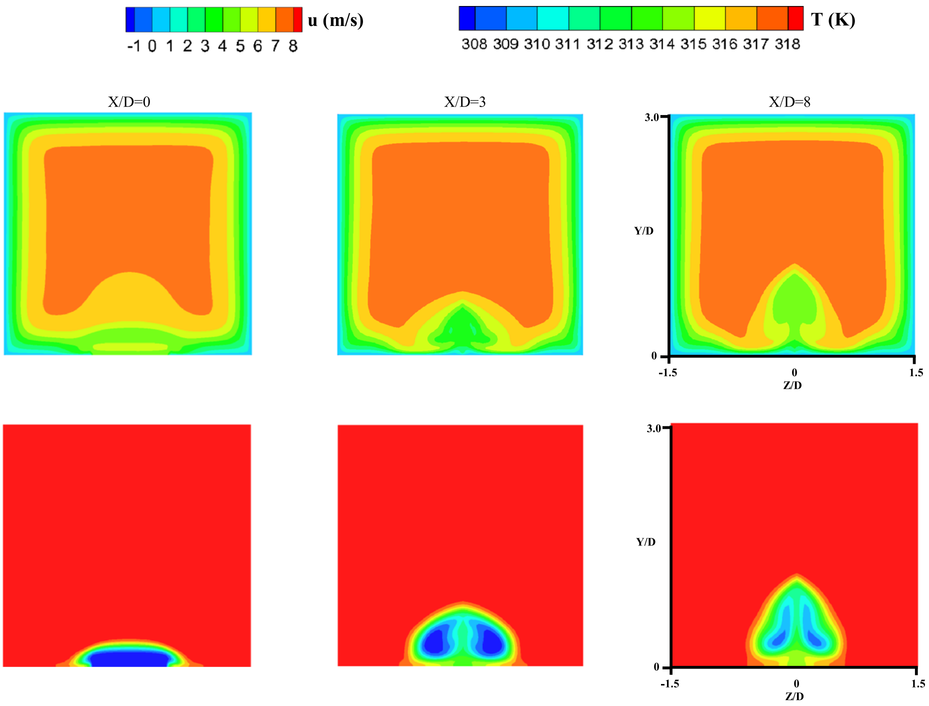

Fig. 8 Time-averaged streamwise velocity & Temperature contours in y-z plane at SN = 0 and Ro = 0.0

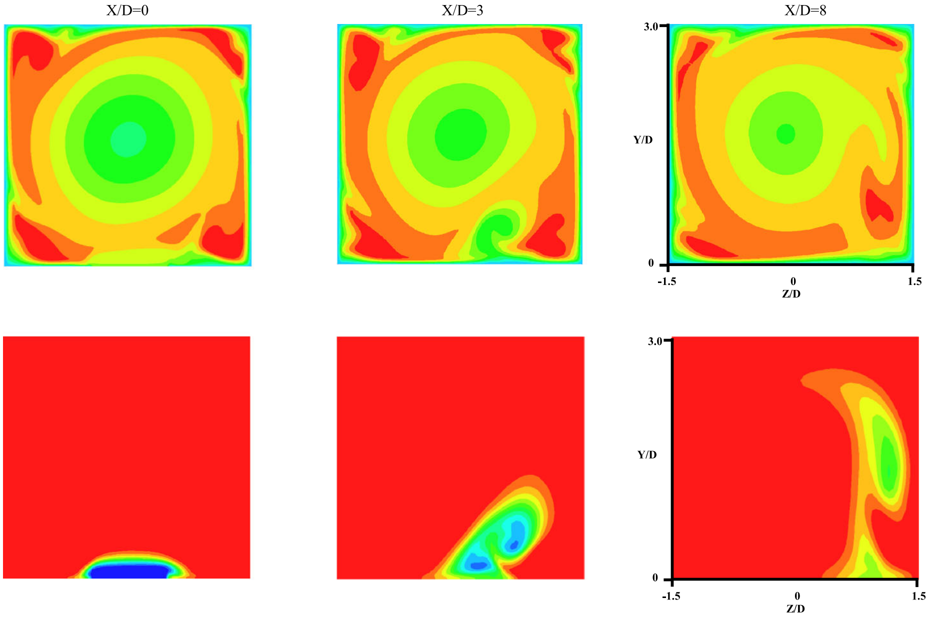

Fig. 9 Time-averaged streamwise velocity & Temperature contours in y-z plane at SN = 0.15 and Ro = 0

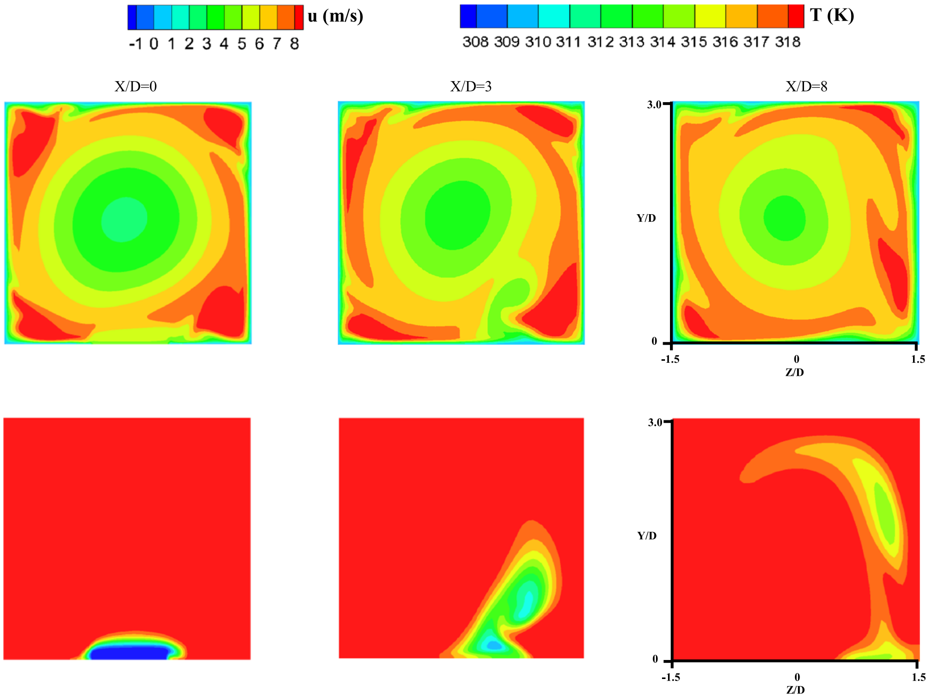

Fig. 10 Time-averaged streamwise velocity & Temperature contours in y-z plane at SN = 0.3 and Ro = 0.0

induced by the rotational movement of swirl flow. Also this force causes the CRVP to rotate around the main vortex core in anti-clockwise direction. No symmetrical kidney shape can be seen downstream of the jet exit, as the main vortex core of the swirl flow moves to the swirl direction and lifts the jet off the lower wall, deforming the kidney shape of the CRVP vortex.

It was found that the velocity profile in the downstream region ($X/D > 3.0$) is nearly symmetrical with respect to the centre of the channel, as opposed to that in the upstream section. It was also found that the swirling flows have the velocity profiles of the forced vortex type and that they decay near the walls downstream.

For $SN = 0.3$ (Fig. 10), the CRVP vortex moves further towards the main vortex core, as the pressure decreases near the core due to the centrifugal effect of the swirling flow. It also appears that the CRVP vortex at $SN = 0.3$ exhibits complex behaviour and has a significant effect on the main vortex shape. For high values of swirl number ($SN > 0.3$), the swirl flow's centrifugal force effect increases; this may reduce the jet penetrations and ultimately decrease the film-cooling effectiveness.

In addition, the horseshoe vortices can be seen in the same figures. These vortices are located down the CRVP at the left and right corners of the y-z planes. For $SN = 0$, the strength of the CRVP increases as the jet penetrates further into the cross flow. Therefore, the HSVs can be pushed towards the lateral boundaries by the CRVP vortex. For $SN > 0$, the interactions between the main vortex and the horseshoe vortices at the corners is quite different. It can be observed that the behaviour of the HSVs at the corners is highly dependent on the locations of the main vortex core; their sizes and intensities are changeable depending on the locations of the main vortex core.

4.2 The effects of rotation

In the presence of rotation effects, the cooling effectiveness is not only determined by the lateral spreading of the coolant jet, but also influenced by the jet trajectories, which are decided by the centrifugal induced buoyancy force and the Coriolis force. These forces alter the movement of the main flow and generate strong secondary flow. The contour lines of the time-averaged streamwise velocity and temperature distribution for $Ro = 0.06042$, 0.12084, and 0.18126 at $SN = 0.15$ are presented in Figs. 11, 12, and 13. They show that both the Coriolis and centrifugal induced buoyancy forces have an impact on flow field and temperature distribution. At $X/D = 0.0$, almost no variation in density is observed. Once the jet begins to penetrate the cross-flow, CRVP and HSVs appear, and their presence causes the jet to mix with the cross-flow downstream of the jet exit. The mixing of the cross-flow and the jet follows the development of the vortex pair and produces a variation in the density downstream of the jet exit. Thus, the low-density fluid is lifted off the surface by the effect of CRVP, leading to a reduction in the film-cooling effectiveness. The "lift off" effect on the low density flow caused by CRVP increases greatly as Ro increases, due to the Coriolis and centrifugal induced buoyancy forces effects. At a low rotational speed ($Ro = 0.06042$), as shown in Fig. 11, the Coriolis and centrifugal induced buoyancy forces may drive the film path slightly towards the right side of the channel, leading to a significant decrease in film-cooling effectiveness. This means that the jet trajectory pushes more to the right side as rotational speed increases.

The buoyancy force always acts in centrifugal direction because the density of cooling air is higher than that of mainstream. For the higher values of Ro, the Coriolis force prevails over the centrifugal force near the film hole. Therefore, the Coriolis force decides that the film trajectory bends centrifugally (if $\Omega > 0$) or centripetally (if $\Omega < 0$). In the present

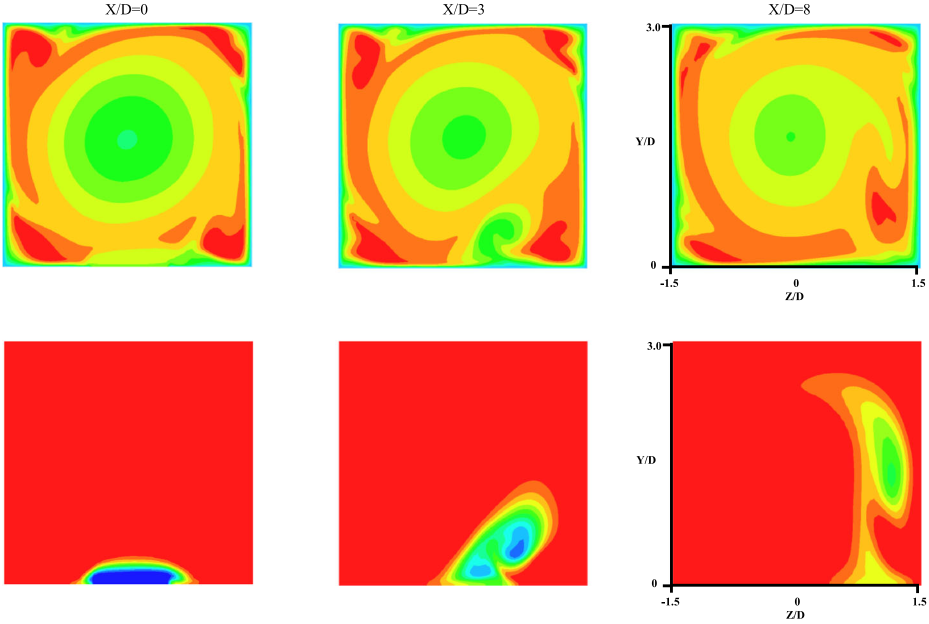

Fig. 11 Time-averaged streamwise velocity & Temperature contours in y-z plane at SN = 0.15 and Ro = 0.06042

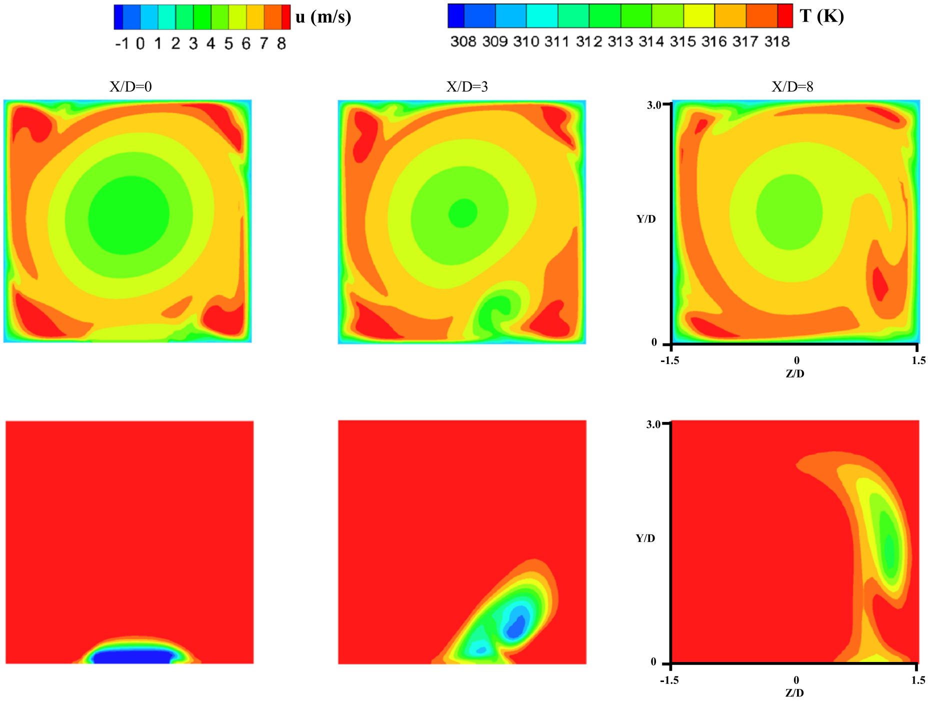

Fig. 12 Time-averaged streamwise velocity & Temperature contours in y-z plane at SN = 0.15 and Ro = 0.12084

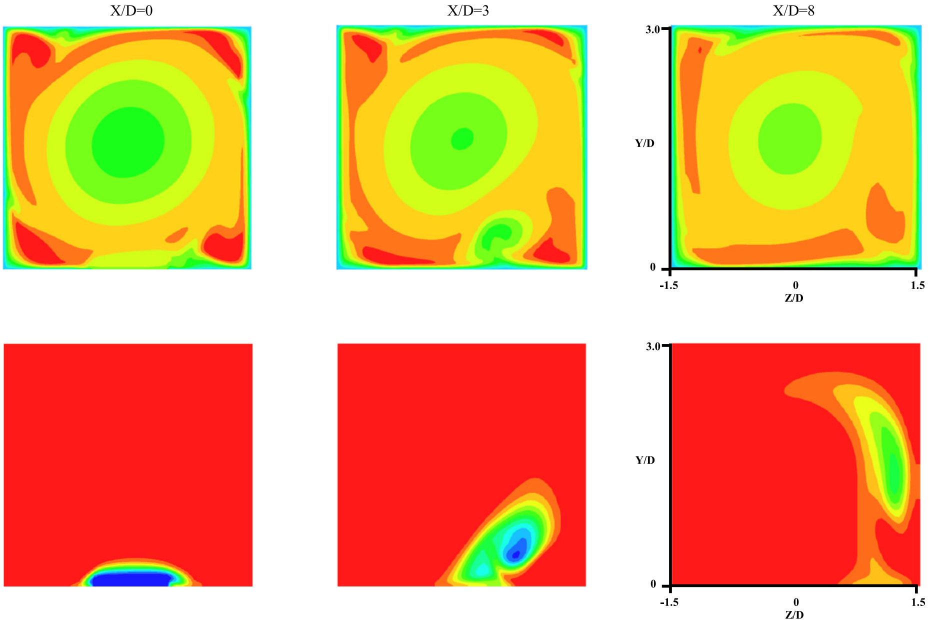

Fig. 13 Time-averaged streamwise velocity & Temperature contours in y-z plane at SN = 0.15 and Ro = 0.18126

study, the rotational speed Ω is always > 0, therefore, the film trajectory always inclines centrifugally and the deflection becomes greater with the increased rotational speed, which attributed to that the Coriolis force acts in the centrifugal direction, as can be clearly seen from Figs. 11–13. As Ro increases further, the Coriolis force tends to dominate the film movement and lifts it off the wall and disturbs the symmetrical shape of the vortices, as shown in Fig. 13.

For SN = 0, the CRVP approaches the left boundary and pushes the HSVs towards the wall as Ro increases. The recirculation region downstream of the jet shrinks as the rotation number increases. The impact of the recirculation in the wake region vanishes when Ro is increased to 0.18126. In addition, the CRVP touches the left boundary at X/D $>$ 8.0 for Ro = 0.18126 and SN = 0 and at X/D $>$ 5.0 for SN = 0.3. Also, the locations of the HSV centres move in Y-direction as Ro increases.

4.3 Turbulent fluctuations

The root mean square (rms) values of the turbulent fluctuations are calculated using the following definition:

$$\left\langle u_i' \right\rangle_{rms} = \sqrt{\left\langle (u_i(x, y, z, t) - < \bar{u}_i > (x, y, z))^2 \right\rangle} \tag{9}$$

Figures 14 and 15 show the distributions of the streamwise turbulent intensity (u_{rms}) for different values of X/D, SN, and Ro at Z/D = 0.0. For SN = 0, it is clearly seen that the highest turbulence levels are located in the shear layer between the recirculation region and the injection hole. In this area, the turbulent boundary layer is lifted by the jet penetration and starts to interact and mix with it, which produces the highest level of fluctuations downstream of the hole.

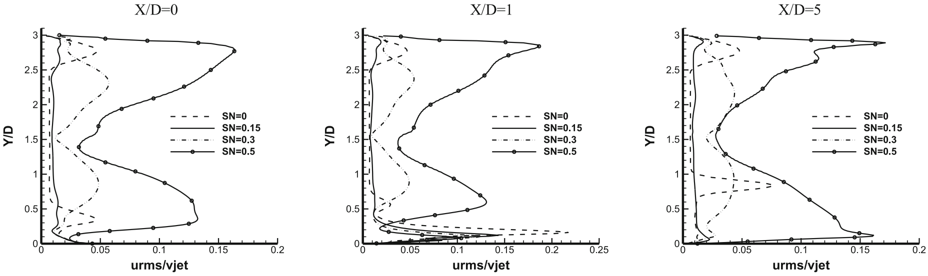

Fig. 14 Distributions of the streamwise turbulence intensity in the symmetry plane at different streamwise locations and Swirl numbers for Ro = 0.0

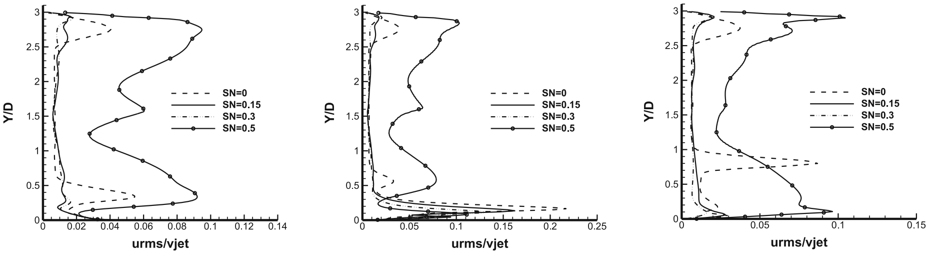

Fig. 15 Distributions of the streamwise turbulence intensity in the symmetry plane at different streamwise locations and Swirl numbers for Ro = 0.12084

For SN > 0, the turbulence levels are located throughout the normal direction and increase in the streamwise direction, as the interaction between the swirl flow and the jet creates a secondary vortex and pushes it to rotate in anti-clockwise direction. It also can be seen from the above figures that turbulence levels are quite high in the core area. This behaviour is caused by the centrifugal force effect of the swirl flow.

The turbulent intensity for the non-rotating case varies symmetrically around Y/D = 1.5 at X/D = 0.0, whereas the profiles for the rotating cases become increasingly asymmetric with increasing rotation number. However, it should be emphasized that the streamwise turbulent intensity is aligned with the axis of rotation and the streamwise fluctuations can therefore not be directly affected by the Coriolis force.

4.4 Film-cooling effectiveness

The film cooling effectiveness (η) can be calculated from the temperature values as follows:

$$\eta = \frac{T_{wall} - T_{\infty}}{T_{jet} - T_{\infty}} \tag{10}$$

In the present study, the lateral average adiabatic film cooling effectiveness was selected as the key parameter in representing the film cooling performance, it was defined as:

$$\bar{\eta} = \frac{\sum_{i=1}^{n} \eta_i A_i}{\sum_{i=1}^{n} A_i} \tag{11}$$

where $\bar{\eta}$ is the average adiabatic film cooling effectiveness within ±1.5d in lateral direction. In Eq. 11, n presents the number of nodes located in ±1.5d at a certain streamwise location.

Figure 16 presents the profiles of spanwise-averaged film cooling effectiveness ($\bar{\eta}$) downstream the film hole for different values of rotation number and swirl number. The cooling effectiveness is almost unchanged and remains almost 0.4 for the region near the hole with $X/D < 1$ and is decreasing rapidly along the streamwise location. For a constant value of Ro, $\bar{\eta}$ decreases as SN increases as the jet can be twisted by the swirl flow effects in anti-clockwise direction and pushed away from the bottom of the channel as shown in Fig. 16a–d. It was shown that for $SN = 0$, as Ro increases, the value of $\bar{\eta}$ increases as shown in Fig. 16a while for $SN > 0$, $\bar{\eta}$ deceases as Ro increases (Fig. 16 b and c) and was found that the rotation has a slight effect on film cooling effectiveness at $SN = 0.5$ as shown in Fig. 16d. Therefore any increase in the values of Ro beyond (0.18126) would have a slight impact on $\bar{\eta}$.

Also, it was found that $\bar{\eta}$ has the worst levels at $SN = 0.5$ compared with that at lower values of SN. Furthermore, It was concluded that the swirl flow has as strong effect on the film cooling effectiveness for all values of Ro. For $SN > 0.3$, $\bar{\eta}$ decreases rapidly as SN increases

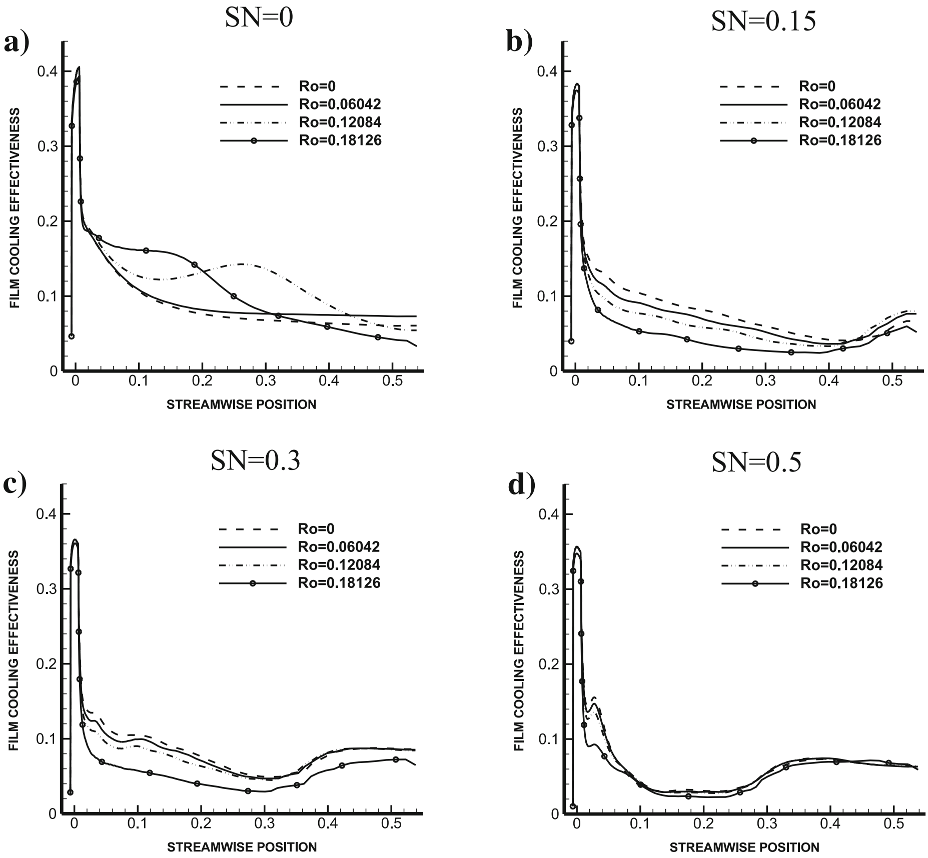

Fig. 16 Spanwise-averaged film cooling effectiveness for different values of Ro and SN

5 Conclusions

The interaction of a jet with a swirling cross-flow was simulated numerically using LES approach for different values of swirl number (SN) = 0, 0.15, 0.3, 0.5, rotation number (Ro) of 0, 0.006042, 0.12084, and 0.18126 with a velocity ratio (VR) of 1.0, and a jet Reynolds number of 4,700. The main conclusions of the present work are:

1. It was found that the swirling flows in the channel have the velocity profile of a forced vortex and show the weak reverse flow near the vortex core.
2. Both swirl and rotation numbers are the most important factors which have strong effects on the jet path direction, jet penetration and mixing progress or, in other words, film cooling effectiveness.
3. It was concluded that film cooling effectiveness is a function of rotation number, swirl number, where the film cooling effectiveness decreases as Ro or SN increases.
4. As swirl number increases, the jet twists increasingly in anti-clockwise direction due to the centrifugal force generated by the swirling flow rotational movement and shifts from the centreline of the channel to the right side (Z/D = + 1.5). The same behaviour was observed as Ro number increases, with the exception of the twisting process.
5. As swirl number increases, the distribution of the film cooling downstream of the jet exit is more non-uniform and the film cooling effectiveness level slightly decreases.
6. It was found that the vortex core of the swirl flow moves in the swirl direction and deforms the kidney shape of the CRVP vortex which appears in the y-z plane.

Acknowledgments The financial support from the Higher committee for education development in Iraq and university of Kufa is greatly acknowledged. Assistances from IT services for running the simulation cases of the present study using CSF cluster at Manchester University, are greatly appreciated.

References

1. Andreopoulus, J., Rodi, W.: Experimental investigation of jets in a crossflow. J. Fluid Mech. **138**, 93–127 (1983)
2. Ajersch, P., Zhou, J.M., Ketler, S., Salcudean, M., Gartshore, I.S.: Multiple jets in a cross flow: Detail measurements and numerical simulations. J. Turbomachinery **1192**, 330–342 (1997)
3. Bosanquet, C., Pearson, J.L.: The spread of smoke and gases from chimneys. Trans. Faraday Soc. **32**, 1249–1263 (1936)
4. Davidson, L., Billson, M.: Hybrid LES-RANS using synthesized turbulent fluctuations for forcing in the interface region. Int. J. Heat Fluid Flow **27**, 1028–1042 (2006)
5. Davidson, L.: Using isotropic synthetic fluctuations as inlet boundary conditions for unsteady simulations. Adv. Appl. Mech. **1**, 1–35 (2007)
6. Ekkad, S.V., Han, J.C., Du, H.: Detailed film cooling measurements on a cylindrical leading edge model: Effect of free-stream turbulence and coolant density. ASME J. Turbomachinery **120**, 799–807 (1998)
7. Farhadi, R., Ramezanizadeh, M., Taeibi, M., Salimi, M.: Compound triple jets film cooling improvements via velocity and density ratios: Large eddy simulation. J. Fluids Eng. ASME **133**, 1–13 (2011)
8. Findlay, M.J., Salcudean, M., Gartshore, I.S.: Jets in a crossflow: Effects of geometry and blowing ratio. J. Fluids Eng. **121**(2), 373–378 (1999)
9. Goldstein, R.J., Eckert, E.R.G.: Effects of hole geometry and density on three-dimensional film cooling. Int. J. Heat Mass Transfer. **17**, 595–607 (1974)
10. Han, J.C., Dutta, S., Ekkad, S.V.: Gas turbine heat transfer and cooling technology. Taylor & Francis, New York (2001)
11. Hoffmann, K., Chiang, S.: Computational Fluid Dynamics, 4th edn. vol. 1. Engineering Education Science 1, USA (2000)

12. Holdeman, J.D.: Mixing of multiple jets with a confined subsonic crossflow. Energy Combust. Sci. **19**, 31–70 (1993)
13. Issa, R.I.: Solution of the implicitly discretised fluid flow equations by operator-splitting. J. Comput. Phys. **62**, 40–65 (1986)
14. Jiang, X., Lai, C.H.: Numerical techniques for direct and large eddy simulations. Taylor and Francis Group, NW (2009)
15. Kristoffersen, R., Andersson, H.: Direct simulations of low-Reynolds-number turbulent flow in a rotating channel. J. Fluid Mech. **256**, 163–97 (1993)
16. Li, S., Li, Z., Guo, T.: Numerical simulation study on the effect of rotation on film cooling of blades with compound angle holes. In: International Conference on ICCE2011, AISC 112, pp. 429–436. Springer-Verlag, Berlin Heidelberg (2011)
17. Ligrani, P.M., Lee, J.S.: Film cooling from two staggered rows of compound angle holes at high blowing ratios. Int. J. Rotating Mach. **2**(3), 201–208 (1996)
18. Molla, M.: LES of pulsatile flow in the models of arterial stenosis and aneurysm. P.hD. thesis, University of Glasgow (2009)
19. Nishiyama, H., Ota, T., Hamada, M., Takahashi, Y.: Temperature fluctuations in a slightly heated slot jet issuing into a crossflow. Exp. Thermal Fluid Sci. **6**, 252–262 (1993)
20. Pedersen, D.R., Eckert, E.R.G., Goldstein, R.J.: Film cooling with large density differences between the mainstream and the secondary fluid measures by the heat-mass transfer analogy. ASME J. Turbomech. **99**, 620–627 (1977)
21. Peyret, R.: Handbook of Computational Fluid Mechanics. Academic, San Diego (1996)
22. Pietrzyk, J.R., Bogard, D.G., Crawford, M.E.: Effects of density ratio on the hydrodynamics of film cooling. ASME J. Turbomach. **112**, 437–443 (1990)
23. Ramezanizadeh, M., Taeibi, M., Saidi, M.H.: Large eddy simulation of multiple jets into a cross flow. Scientia Iranica **14**(3), 240–250 (2007)
24. Renze, P., Meinke, M., Schroder, W.: LES of turbulent mixing in film cooling flows. In: Conference on Turbulence and Interactions. Porquerolles, France (2006)
25. Sinha, K., Bogard, D.G., Crawford, M.E.: Film cooling effectiveness downstream of a single row of holes of variable density ratio. ASME J. Turbomachinery **113**, 442–449 (1991)
26. Smagorinsky, J.: General circulation experiment with the primitive equations. I. the basic experiment. Monthly Weather Rev. **91**(3), 99–164 (1963)
27. Sutton, O.G.: A theory of eddy diffusion in the atmosphere. Proc. Roy. Soc. A **135**, 143–165 (1932)
28. Tao, Z., Yang, X., Ding, S., Xu, G., Wu, H., Deng, H., Luo, X.: Experimental study of rotation effect on film cooling over the flat wall with a single hole. Exper. Thermal Fluid Sci. **32**, 1081–1089 (2008)
29. Van Driest, E.R.: On the turbulent flow near a wall. J. Aero. Sc. **23**(11), 1007–1011 (1956)
30. Versteeg, H.K., Malalasekera, W. An introduction to computational fluid dynamics: The finite volumes method, 2nd edn. Longman Pearson Education Limited, England (2007)
31. Visscher, J., Andersson, H., Barri, M., Didelle, H., Viboud, S., Sous, D., Sommeria, J.: A new set-up for PIV measurements in rotating turbulent duct flows. Flow Meas. Instrum **22**, 71–80 (2011)
32. Walters, D.K., Leylek, J.H.: A detailed analysis of film-cooling physics: Part I – streamwise injection with cylindrical holes. ASME J. Turbomech. **122**, 102–112 (2000)
33. Yao, Y., Maidi, M., Yao, J.: Effect of jet inclination angle and hole exit shape on vortical flow structures in low-reynolds number jet in cross-flow. Modell. Simul. Eng. **2012**, 1–7 (2012)